




Radiometric Autonomous Navigation Fused with Optical for Deep Space Exploration

Todd A. Ely¹  · Jill Seubert¹ · Nicholas Bradley¹ · Ted Drain¹ · Shyam Bhaskaran¹

Accepted: 7 December 2020 / Published online: 22 January 2021

© California Institute of Technology. Government sponsorship acknowledged. 2021, corrected publication 2022

Abstract

With the advent of the Deep Space Atomic Clock, operationally accurate and reliable one-way radiometric data sent from a radio beacon (i.e., a DSN antenna *or other spacecraft*) and collected using a spacecraft's radio receiver enables the development and use of autonomous radio navigation. This work examines the fusion of radiometric data with optical data (i.e. OpNav) to yield robust and accurate trajectory solutions that include selected model reductions and computationally efficient navigation algorithms that can be readily adopted for onboard, autonomous navigation. The methodology is characterized using a representative high-fidelity simulation of deep space cruise, approach, and delivery to Mars. The results show that the combination of the two data types yields solutions that are almost an order of magnitude more accurate than those obtained using each data type by itself. Furthermore, the combined data solutions readily meet representative entry navigation requirements (in this case at Mars).

Keywords Autonomous navigation · Radiometric tracking · Optical navigation

✉ Todd A. Ely
Todd.A.Ely@jpl.nasa.gov

Jill Seubert
Jill.Tombasco@jpl.nasa.gov

Nicholas Bradley
Nicholas.E.Bradley@jpl.nasa.gov

Ted Drain
theodore.r.drain@jpl.nasa.gov

Shyam Bhaskaran
shyamkumar.bhaskaran@jpl.nasa.gov

¹ Jet Propulsion Laboratory, California Institute of Technology, 4800 Oak Grove Drive, Pasadena, CA 91109-8099, USA

Introduction

With the advent of NASA's Deep Space Atomic Clock (DSAC), operationally accurate and reliable one-way radiometric data sent from a radio beacon (i.e., a DSN antenna *or other spacecraft*) and collected using a spacecraft's radio receiver enables the development and use of autonomous radio navigation [1]. Autonomous navigation using JPL's AutoNav software system has been a critical technology for many deep space missions, including Deep Space 1, Stardust, and Deep Impact [2]. For these missions, autonomous navigation was conducted using passive optical imaging of nearby bodies with an on-board camera system (called OpNav). Optical data provides strong angular information about a spacecraft's 'plane-of-sky' relationship to the object being imaged. Range (or 'line-of-sight') information, orthogonal to the plane-of-sky, is more difficult to determine from optical data due to the slow rate of angular change seen with observed bodies. A more direct measure of line-of-sight is obtained with radiometric tracking of range and Doppler. These measurements complement optical data, and, when combined, yield a more complete *robust solution* for a spacecraft's absolute position in space. Indeed, the *fusion* of these two data types is central to an autonomous deep space navigation capability that would be needed for a wide range of future missions – examples include autonomous landings on solar system bodies, human exploration of the Moon, Mars and beyond, and improved navigation efficiency for orbiters and interplanetary craft.

When considering onboard autonomous navigation, we seek a robust design that maximizes use of simplified models and requires minimal ground-based calibration data. To that end, we apply a recently developed type of radiometric measurement, dubbed one-way charged particle-free (CPF)-phase, that is well suited for onboard use because it eliminates errors induced by Earth-based ionosphere and space-based solar plasma charged particles [1]. We will show that this data type can be readily used for deep space onboard navigation via filter compensation using only long-term model predicts for troposphere and Earth-orientation parameters. Additionally, we will show that, with prudent stochastic modeling, simplified spacecraft dynamics models (even for complex spacecraft that exhibit significant small force perturbations resulting from unbalanced thrusting by the reaction control system) are also viable for extended, convergent use by the navigation filter. We have combined the CPF-phase data with onboard imaging of asteroids to determine an accurate, and robust trajectory determination capability that could be used to target entry or orbit insertion at planets, such as Mars. Finally, we examine two approaches towards filtering: one using an iterated linearized-Kalman filter with mapping (vs smoothing) and the other using an extended Kalman filter that employs a moving batch window. Both approaches support trajectory knowledge updates at atmosphere entry that can be used by an onboard guidance system to flyout delivery errors whereas ground-based navigation updates typically occur hours prior to entry.

We apply the CPF-phase model because it promises to be a general-purpose radiometric observable that could prove to be suitable anywhere in the solar system for onboard deep space navigation while requiring only minimal calibration information. We also augment the CPF-phase data with onboard optical data to provide improved geometric observability and to ensure that the navigation solutions are strongly sensitive to the target destination. Radio data could serve this purpose if there

were an emplaced tracking infrastructure at the destination of interest, which may be true in the future at a destination like the Moon or Mars, but will not in general be true elsewhere in the solar system. Optical imaging of a target destination is, by definition, directly sensitive to the target and aids navigation as the spacecraft approaches it. Additionally, the filtering approaches we propose have been used successfully for decades in ground-based navigation but modified for onboard use by eliminating smoothing, thus greatly reducing the operational memory requirements needed. To make the case for these findings we structure our study around a Monte Carlo investigation of a realistic Mars navigation scenario. We have selected this because it is a high interest use case, as well as fundamentally acknowledges that any reduced-order model implementation of an onboard deep space navigation system will necessarily be tailored to the mission at hand. Hence, while the dynamic model reductions utilized for the current case may not apply to another completely different application (say, for instance, a small body tour in the asteroid belt), it does represent an existence proof that using the combined radio and optical data with the filter method proposed is sufficient for onboard autonomous navigation for an important case.

Fundamental to any Monte Carlo investigation to confirm reduced-order navigation models and approaches requires development of a realistic, high-fidelity ‘truth’ model that represents the expected perturbations to a reference trajectory, the response to these perturbations with trajectory correction maneuvers, and, ultimately, simulation of a set of observables that reflect this truth model. That is, we will simulate streams of ‘truth’ measurement data and then process that data on the ‘nominal or reference’ side using the reduced-order models and the orbit determination filter methods proposed for the onboard navigation system, and do so with a statistically significant sample size to make meaningful determinations on the effectiveness of the models and filters. We structure our approach by first developing the CPF-phase model in some detail, review the OpNav approach, then describe the Mars use case and the specific model adaptations selected for the case, and the describe the filter methods studied. Finally, the Monte Carlo simulation results are presented.

Onboard One-Way Radiometric Measurement Models and Considerations

Determining an accurate spacecraft trajectory requires several characteristic features from the measurement data: accuracy, precision, diversity, and density. For one-way data, a stable and accurate clock plays a critical role with the first two items – accuracy and precision. Diversity and density, while also impacted by onboard clock stability and accuracy, rely more on the characteristics of the trajectory and radio tracking sources. Other key factors relate to model uncertainties and their associated stochastic behavior. All of these issues will be explored when using DSAC as part of an autonomous navigation system, but to begin, we consider the model for several one-way radiometric measurement types.

A robust onboard navigation system needs to maximize self-reliance, and be able to operate for extended periods without calibration and/or model updates. Calibration data that requires significant ground support, or cannot be obtained in real-time, would limit that measurement’s utility to support autonomous navigation. Specifically, current high-fidelity

ground-based two-way radiometric data requires atmospheric media (troposphere and ionosphere) delay data, high precision Earth orientation data, and range bias data to support precision orbit determination. One of the most significant error sources for radiometric data is from charged particle effects (i.e., ionosphere and/or solar plasma) [3]. In this study we use a derived one-way radiometric data type, called charged particle-free-phase or CPF-phase, that minimizes these effects. The model for CPF-phase was first developed in Ely, et al. [1] and is presented here for completeness. We also develop a set of calibration approaches and/or filter compensations that are sufficiently accurate for weeks to months at time; hence minimizing the need for frequent or even daily data calibrations (as would be required with existing data types and models).

One-way CPF-phase $\Phi_{CPF}(t)$ is a linear combination of the traditional one-way phase $\Phi(t)$ and one-way range $R(t)$ measurements. The one-way phase is a measure of the difference of two clock signals (called the beat signal and denoted as $\Delta\phi(t)$) with one being the phase of a received radio transmission and the other being the phase of a locally generated signal within the radio receiver. Without loss of generality, all of the radiometric models considered in this paper are for one-way data types that originate from a radio source (ground station, or other satellite) and are received onboard the spacecraft of interest. As will be seen, this implies that the spacecraft clock (such as DSAC) participates in formulating the measurement and ‘tagging’ its associated time. Two-way radiometric models are similar, but distinct. Receiver R ’s beat phase of $\Delta\phi(t)$ at the ideal time t is formed as the difference of the transmitted phase ϕ_T from transmitter T and the receiver’s reference phase ϕ_R and takes the form

$$\begin{aligned} \Delta\phi(t) &= \phi_T(t-\tau) - PW(t) - \phi_R(t) \\ &= -f_T\tau - f_T[x_R(t) - x_T(t-\tau)] - PW(t) \end{aligned} \tag{1}$$

where $PW(t)$ represents the ‘phase wind-up’ that results from the relative orientation changes between the receiving antenna and the transmitting antenna, f_T represents the transmission frequency (for simplicity, any frequency bias that might exist with a mismatch between transmission frequency f_T and the receiver frequency f_R has been set to zero). A clock’s time deviation x from ideal time t is related to its phase using $\phi = f(t - x)$; thus, x_R is defined as the receiver clock’s time deviation, and x_T is the transmitter clock’s time deviation. The quantity τ is the one-way light time delay from the phase center of the transmitting antenna to the phase center of the receiving antenna and is defined as

$$\tau \equiv t_R - t_T = t - t_T \tag{2}$$

where $t \equiv t_R$. The delay includes the geometric path length $\Delta r(t)$ as well as delays from other effects including ionosphere $I(t)$, solar plasma $S(t)$, and the troposphere $T(t)$, yielding

$$\tau(t) \cong \frac{1}{c} (\Delta r(t) - I(t) - S(t) + T(t)) \tag{3}$$

where, for phase observables, the ionosphere and solar plasma delays appear to ‘shorten’ the path length; thus, the minus sign (in range observables these delays will

‘lengthen’ the path length).¹ In practice, accurate computation of the geometric path length $\Delta r(t)$ must include the full spacetime geometry effects due to special and general relativity and complete expressions for these can be found in Moyer [4]. Conceptually, the geometric path length $\Delta r(t)$ path length is most easily understood via its Newtonian approximation, which takes the form

$$\Delta r(t) \cong \|\mathbf{r}_R(t) - \mathbf{r}_T(t - \tau)\|. \quad (4)$$

The vectors \mathbf{r}_R and \mathbf{r}_T represent the position of receiving antenna’s phase center and transmitting antenna’s phase center, respectively. Note that the preceding model is generic and the presence of the ionosphere, solar plasma, and troposphere delays are dependent on whether the signal transits through the respective media. Their computation is also dependent on the appropriate time of transit; thus, an uplink signal from the Earth to a spacecraft receiver would evaluate the ionosphere and troposphere transit at the time $t - \tau$. For this discussion the functional representation of these delays on t is sufficient, where a more specific calculation must be made at the appropriate time and/or functional dependency on environment parameters would be substituted.

A receiver measuring the beat phase given in Eq. (1) will introduce other errors such as: instrument delays, noise, potentially multipath effects, and an integer ambiguity (representing the number of complete cycles that have occurred since the signal left the transmitter at the start of the tracking pass). These considerations result in the following one-way phase measurement model (converted into units of length)

$$\begin{aligned} \Phi(t) &\equiv -\frac{c}{f_T} \Delta\phi(t) \\ &= \Delta r(t) + c[x_R(t) - x_T(t - \tau)] - I(t) - S(t) + T(t) + PW(t) + M^\Phi(t) + b_R^\Phi(t) + b_T^\Phi - N + \nu(t) \end{aligned} \quad (5)$$

where $M^\Phi(t)$ is the error due to multipath effects, $b_R^\Phi(t)$ is the receiver delay, b_T^Φ is the transmitter delay (assumed static in this discussion, i.e., $\dot{b}_T^\Phi = 0$), N is the integer phase ambiguity, and $\nu(t)$ is the one-way phase measurement noise. It should also be noted that the receiver records the measurement with time tag $C(t)$. One-way range collected by a spacecraft receiver has a model that is very similar in form to the carrier phase model in Eq. (5) and is formally represented using

$$R(t) = \Delta r(t) + c[x_R(t) - x_T(t - \tau)] + I(t) + S(t) + T(t) + PW(t) + M^R(t) + b_R^R(t) + b_T^R + \varepsilon(t) \quad (6)$$

where the differences between the range expression in Eq. (6) versus the phase in Eq. (5) include sign changes on the ionosphere and solar plasma delays, different receiver delays $b_R^R(t)$ (including temperature sensitivities), multipath $M^R(t)$, measurement noise $\varepsilon(t)$, and no phase ambiguity. Additionally, since our application is for one-way radiometric data processing onboard a spacecraft, we have developed a high-fidelity model of representative onboard oscillator/clocks such as NASA’s DSAC, an Ultra Stable Oscillator (USO), or Microchip’s Chip Scale Atomic Clock (CSAC). As documented in Ely [6], these onboard

¹ As explained in Hofmann-Wellenhof, et al [5], a electromagnetic signal in a frequency dependent dispersive media (i.e., ionosphere or solar plasma) produces a positive group delay for ranging code phases and a decrease in wavelength yielding a decrease in an integrated carrier phase.

clocks have unique characteristics that must be accounted for in an onboard radiometric observable model and the associated navigation filter that will process this data. In particular, USOs and CSAC both have long term drift and stochastic instability characteristics that reduce the accuracy of one-way radiometric data relative to its two-way counterpart that must be modeled to obtain correct navigation solutions and, because of these characteristics, often degrading the accuracy of the solutions. On the other hand, DSAC stability is orders of magnitude better than CSAC and, on timescales longer than several tens of seconds, better than the most stable USO. As a result, one-way radiometric measurements obtained from a receiver using DSAC as a reference exhibit accuracy that is on par with the equivalent two-way radiometric data.

As with their two-way counterparts in use today, the preceding one-way data types are sufficient in their expressed forms for use in high precision deep space navigation, but they, like the two-way data, would require daily calibrations for media delays and Earth orientation to be useful. For onboard use, it is beneficial to minimize the need for frequent calibration data updates. An immediate consequence of the forms of Eqs. (5) and (6) is, via a linear combination of the measurements, charged particle effects from the ionosphere and solar plasma can be removed. In particular, we define the charged-particle-free (CPF) phase using

$$\Phi_{\text{CPF}}(t) \equiv \frac{R(t) + \Phi(t)}{2}, \quad (7)$$

where the resulting model takes the form

$$\begin{aligned} \Phi_{\text{CPF}}(t) = & \Delta r(t) + c[x_R(t) - x_T(t - \tau)] + T(t) + \frac{PW(t)}{2} + \langle M(t) \rangle + \langle b_R(t) \rangle \\ & + \langle b_T \rangle - \frac{N}{2} + \frac{\varepsilon(t) + \nu(t)}{2}. \end{aligned} \quad (8)$$

Note that neither charged-particle delays from the ionosphere nor solar corona plasma effects are present. This eliminates the need to calibrate for these at the expense of an increased overall noise relative to the phase by itself (DSN-based range measurement noise typically is 1 to 3 m (1- σ) while the phase noise is 5 mm (1- σ)). More importantly, the measurement noise is white, while charged-particle stochastic effects are correlated and have difficult-to-model temporal effects (such as the day/night cycle). Simpler white noise stochastic modeling yields a more robust filter than one with complex time dependent stochastic models that require careful tuning (and that may change over time) for obtaining convergent and correct trajectory solutions.

The effects of the phase ambiguity term can be minimized to the level of the range error via using the range measurement value at the beginning of a pass to calibrate for the ambiguity.² This has the subtle effect of ‘pushing’ range errors (including charged-

² Note that as an alternative to phase, forming a one-way Doppler measurement using consecutive CPF-phase measurements could be utilized as it would eliminate the need to determine a phase ambiguity; however, this would also significantly reduce the sensitivity to the initial clock bias making it more difficult to determine accurately. A topic of a future study would be to compare use of CPF-phase relative to one-way Doppler derived from this data.

particle effects and initial clock offsets) into the range bias, but in a typical multi-hour pass static range biases are observable (defined as the filter recovering the injected range bias with errors that are consistent with its estimated uncertainty) and have been confirmed in the results to be presented. The largest error in the rescaled bias is an unknown clock bias contained in $x_R(t)$ of the onboard clock. A first estimate of this bias can be ascertained early in the orbit determination process using a separate clock-only estimator using differences of two-way and one-way range and Doppler data types. With DSN range data precision at the several meter level it is reasonable to determine initial clock offsets to $<1e-6$ s and with Doppler data types at <0.1 mm/s (typical of the DSN at X-band) clock rates to $\sim 1e-14$ using data differencing techniques and averaging. Once the clock offset and rate are known, DSAC stability is sufficient to enable processing the one-way data types similar to their two-way counterparts without additional clock compensation in the filter (other than estimating the clock bias states with constrained a priori uncertainties). Additionally, two-way data types would no longer be needed, and mission navigation could proceed with using the one-way CPF data type (as will be seen in later analysis). For other choices of clocks (such as a USO or a CSAC) this would not be the case, and specific stochastic process filter compensations would be required with periodic clock recalibrations needed. For this analysis, use of DSAC is assumed. After correlating for the spacecraft clock, a conservative bound for the range bias uncertainty (including charge particle delays at X-band) is 3 m (1-sigma).

Even though CPF-phase removes the first-order effects of charged particles, other delays and errors remain that need to be addressed, including atmospheric troposphere delays and high precision Earth orientation parameters:

1. Unlike ionosphere and solar plasma effects, troposphere daily effects (on the order of a ~ 5 cm delay) are readily dealt with using an appropriately tuned stochastic model or via increasing the measurement uncertainty of the CPF-phase data. What remains is a seasonal troposphere delay that can be calibrated using a compact model in the onboard orbit determination models [7]. A stochastic model for these delays has been developed by analyzing the statistics (including Allan deviations) of several months of dry and wet troposphere measured delays, and is in the model provided in Table 1. Both the wet and dry delays conformed to a first-order Gauss-Markov process (ECRV) with differing strengths and timescales as listed in the table.
2. The remaining real-time model considerations are the high precision Earth orientation models and their impact on an onboard implementation when daily calibrations for, primarily, Earth pole motion and UT1 time drift are not available (as would be the case for long periods of autonomous operations). Kalarus, et al. [8] have thoroughly documented the characteristics of the high precision Earth orientation calibrations available from the International Earth Rotation Systems Service (IERS) for reconstruction and prediction (for periods of up to 500 days). They find that both pole motion and UT1 predict errors grow unbounded to levels near 8 mas and 4 ms (1σ) at 30 days, respectively. On a 500-day prediction interval, the errors grew to 80 mas for pole motion and 80 ms (1σ) for UT1. A real time,

Table 1 Truth Models for CPF-phase and Associated Earth-centric Model Effects

Parameter	Truth Model including Injected 1σ Errors
Phase noise	White noise at 4.24 mm
Range noise	White noise at 1 m
Range Bias	2 m bias applied at start of each DSN pass + ionosphere effects at X-band from observed delays
Clock Bias	1.e-6 s (assumes clock calibration)
Frequency Bias	1.e-14 (assumes clock calibration)
Stochastic Frequency	White Frequency (WF) Noise Sequence with $AD = 3e-15$ @ 1-day
Earth troposphere delays	Long period model effects Daily Dry Delay ECRV = 2 cm with $\tau = 3$ h Daily Wet Delay ECRV = 5 cm with $\tau = 0.75$ h
Earth UT1 errors	Random walk with $\sigma(30 \text{ days}) = 4$ milli - seconds
Earth (X, Y) pole motion errors	Random walk with $\sigma(30 \text{ days}) = 8$ milli - arcseconds
Station Locations	Surveyed DSN station locations located in a high precision Earth body fixed frame with precision, nutation, UT1, and pole motion effects with injected errors consistent with the fully correlated station covariance

onboard autonomous navigation system might have to utilize predictive models for months at a time (depending on the specific mission context). As with the troposphere delays, the random walk stochastic models listed in Table 1, based on Kalarus, et al. [8], were compared to several months of differences between UT1 and pole-motion actual and predicted values with the stochastic model yielding conservative bounds. With this filter-based model compensation, it is sufficient to model the Earth orientation using the International Astronomical Union (IAU) frame definitions [9] which can be easily implemented for onboard use.

Earth station locations located on a high precision frame have been replaced with Chebyshev fits of data and placed into the IAU Earth Fixed frame. These fits can be accomplished to a prescribed accuracy. For the current application, all three participating DSN stations have been fit to better than centimeter accuracy with the resulting two-month station ‘trajectories’ taking only 76Kb of space. In summary, the CPF-phase data type is ideal for onboard, autonomous use because it inherits the fundamental precision of the DSN radiometric data types (at approximately 50 cm) and only requires calibration models that can be predicted for months ahead – that is, no daily calibration data is needed.

The truth models and associated errors used to generate the CPF-phase measurement realizations for the later Monte Carlo studies are summarized in Table 1. Later tables will provide the associated modeling and filter design used for the onboard navigation.

Onboard Optical Imaging (OPNAV)

Recently, Broschart, et al. [10] did an exhaustive study of kinematic positioning in the solar system using camera images (also known as OpNav) of main belt asteroids and

developed a heuristic algorithm for selecting asteroids that could be adapted for use in autonomous deep space navigation to define asteroid imaging schedules. The algorithm factors asteroid brightness, camera quality, and asteroid location uncertainties to determine which asteroids to image based on certain heuristic cost functions. Part of the work surveyed the distribution and characteristics of the asteroids for use in navigation. Some particular features that are noteworthy include:

1. There are over 50 K known and mapped bright main belt asteroids with magnitudes (M) < 14.9; hence, making them potential targets for navigation grade cameras and to use as optical ‘beacons’ for navigation.
2. These asteroids are between 2 and 4 AU from the Sun and have a typical position uncertainty of <100 km, and almost all are <200 km. The asteroid ephemerides are sufficiently well known that this error is commensurate or smaller relative to other errors.

Additionally, representative navigation cameras examined by Broschart, et al. [10] could be lumped into three categories consisting of low-end, mid-range, and high-end camera features as noted in Table 2. FOV is the camera field-of-view, Θ is field of view of one camera pixel (called the IFOV), M_{\max} is the maximum apparent magnitude of the asteroid that can be detected, ψ_{\min} is the minimum allowable sun-spacecraft-asteroid angle allowable. Finally, the camera pixel array’s horizontal and vertical measurement uncertainty σ_s , selected for each camera was 0.25 that is a conservative bound factoring errors from in center finding, camera calibrations, and camera pointing.

For the current study, we have selected a gimballed, high-end camera system to pair with the CPF-phase measurements. When the camera images an asteroid it will be projected onto its 2-d focal plane that is then digitally sampled by an array of detectors. This results in a set of horizontal and vertical coordinates for the center of figure of all the detectable asteroids (and other bright bodies) in the camera’s field of view. The pixel coordinates of an asteroid, coupled with asteroid ephemeris knowledge, and camera pointing can be used to determine the spacecraft position relative to the imaged bodies; thus, using it for spacecraft navigation. The optical measurement model adapted for use is documented by Owen [11] and is part of the JPL’s operational Monte navigation software system [12–14]. The use of the gimbal enables the spacecraft to point the camera without changing attitude, thus enabling the spacecraft to image as needed without interrupting other operations. Prior onboard operational experience with optical data has shown that, in most cases, the image pointing direction can be ascertained using the known star background to a micro radian accuracy [15]. This has been assumed in our simulation with pointing errors injected at this level. Use of this

Table 2 Range of Optical Camera Properties [10]

Navigation Camera Class	FOV (deg)	Θ (μrad)	M_{\max}	ψ_{\min} (deg)
Low-end	26.9	128	9.5	30
Mid-level	7.0	60	10.5	30
High-end (selected for this study)	0.6	10.0	13.5	30

approach also implies that attitude information is not required; however, in the event that orientation determination is not possible an explicit interface to the spacecraft for its attitude and the camera gimbal pointing angles would be needed. Also, for this study we are only imaging bodies that appear as point sources in the focal plane (i.e., they are distant enough that the center of figure can be determined easily within a pixel). Asteroid ephemeris errors are included in the simulated truth trajectories for the asteroids while the onboard filter model will either ignore these errors (when processing both CPF-phase and OpNav data) or consider them (when processing OpNav data only).

Onboard Model Considerations and Filter Design Using a Mars Navigation Case Study

In addition to minimizing the need for frequent calibration data updates, another objective in implementing an autonomous navigation system is to minimize model complexity to reduce computational burden while still maintaining sufficient trajectory accuracy and solution robustness. For example, high fidelity ground-based deep space navigation utilizes complex spacecraft shape models and reflective properties to accurately capture solar radiation pressure effects. Beyond complexity, these models are also dependent on having knowledge of spacecraft attitude at all times to accurately determine solar radiation pressure forces. As a potential onboard model simplification, we consider the possibility of replacing an attitude dependent, complex spacecraft shape model with a simpler attitude-free, average solar-oriented area and compensate for the fidelity reduction using process noise acceleration parameters in the navigation filter to maintain convergence. We also explore the question of whether a simple generic three-axis stochastic acceleration can be used to maintain filter convergence in the presence of unknown small accelerations that result from having imperfect model information. We address the feasibility of this, other reduced-order model considerations, and navigation filter design by focusing on a realistic scenario of navigating a spacecraft to Mars.

The late-cruise, approach, and entry navigation of the recent Mars InSight lander is a representative (and extensible) use case for determining a set of models and developing a navigation filter design that would be suitable for onboard navigation. We select this because it is a mission that demonstrates the state of the art in deep space navigation, and there is a wealth of recent data for use in validating our results. Our truth simulations use the models and error assumptions that the InSight navigation team utilized in their navigation system design as documented by Abilleira [16] with the exception that the reaction control system (RCS) small forces values selected for this study were used earlier in the project. The nominal InSight trajectory for launch on May 5, 2018 is shown in Fig. 1. We have selected the last 45 days (after TCM-3) and ending at entry (defined at a 126 km altitude and nominally with a Mars centered, inertial speed of 5.76 km/s) as the period for our investigation since this represents the most dynamic phase of the trajectory where specific entry flight path angle constraints need to be achieved. In particular, InSight's delivery and knowledge requirements were:

Launch = 05/05/2018
Arrival = 11/26/2018

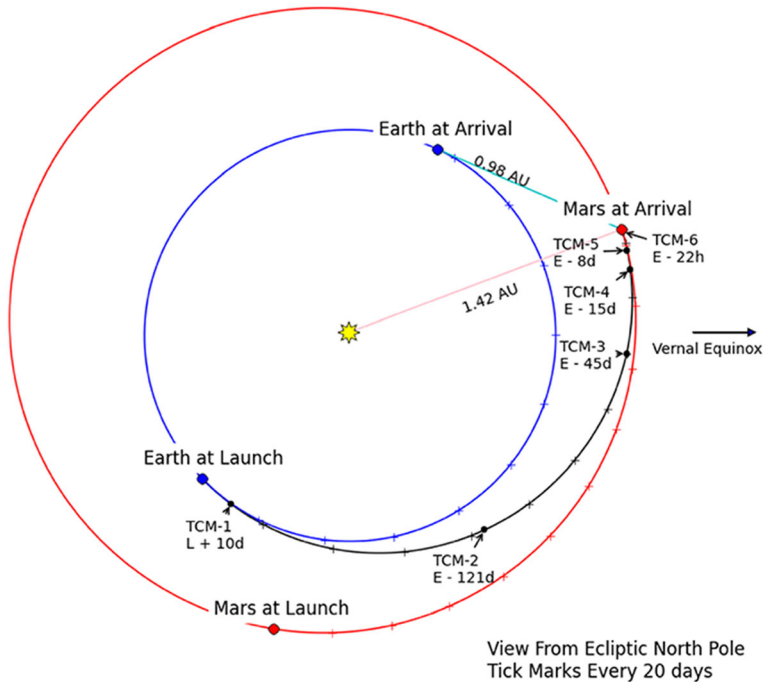


Fig. 1 InSight trajectory for launch on May 5, 2018 from Abilleira [16]. The period of investigation in this study is the last 45 days beginning after TCM-3 and ending at entry on Nov 26, 2018

1. Delivery entry flight path angle (EFPA) should be $-12^\circ \pm 0.21^\circ$ ($3\text{-}\sigma$),
2. Knowledge of the delivered EFPA must be within $\pm 0.15^\circ$ ($3\text{-}\sigma$).

Using simulated truth trajectories and measurement data derived from the InSight models we have been able to develop autonomous navigation model and filter designs to achieve InSight's Mars atmosphere delivery objectives while minimizing model complexity and retaining solution robustness. Indeed, the navigation simulation tool used to develop the autonomous navigation model and filter designs was validated using the InSight navigation plan results and the associated high-fidelity models available in Monte. In the remainder of this section we analyze the specific adaptations needed for an onboard autonomous navigation to be able to support deep space navigation in at least the Mars navigation case being considered here.

Simplifying the Spacecraft Shape and Associated Solar Pressure Modeling

The pre-launch high-fidelity InSight shape model consists of many components that require their own reflectivity parameters and nominal orientations.³ The shape model has five

³ During actual flight, the InSight navigation team switched the SRP model from a component model to one based on spherical harmonics.

components representing the solar arrays, the launch vehicle adapter on the cruise stage, the cruise stage outer ring, and the backshell (two components). The InSight cruise configuration is illustrated in Fig. 2. The models include diffuse and specular reflectivity coefficients for each component. For the period being investigated, InSight maintains its orientation such that the normal to the solar arrays is oriented towards the Sun while still allowing access to the Earth via the MGA. The result is a relatively constant solar oriented area, which suggests that an aggregate area, single component spherical shape might be adequate for an onboard spacecraft shape representation. In addition to its simplicity, this model is also attractive as it is independent of attitude, thus eliminating the need for real-time attitude information from the spacecraft. For the InSight example, assuming a constant solar-oriented area yielded three axis solar radiation pressure accelerations that differed from the truth by less than 1.5% resulting in acceleration difference magnitudes of $<5e-13$ km/s [2]. The acceleration differences exhibited biased values in each direction (i.e., non-zero mean value) with aperiodic variations around each bias. This suggests that a bias and stochastic acceleration model might support compensation for these differences, which is explored and confirmed in this study.

Small Forces Modeling

Because the InSight cruise stage maintains attitude with a three-axis unbalanced thruster control system, there are numerous (almost continuous) small translational

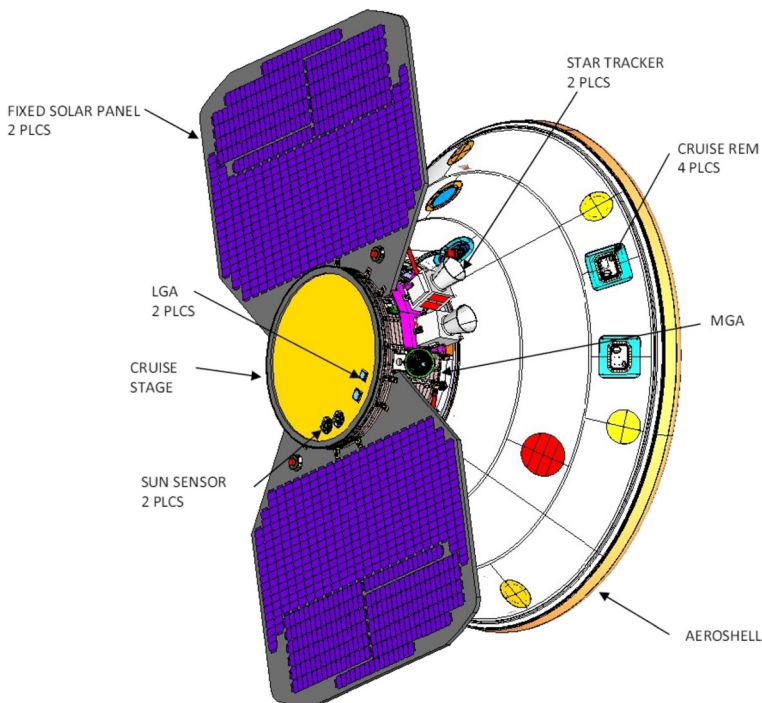


Fig. 2 InSight Cruise Configuration [16]

Table 3 Truth Dynamic Models for the Mars Approach Spacecraft

Parameter	Truth Model	Injected Error (1σ)
Initial Position	Targeted for each simulated truth trajectory to achieve Mars entry conditions.	10 km (consistent with a converged handoff from ground-based navigation)
Initial Velocity	Targeted for each simulated truth trajectory to achieve Mars entry conditions.	1 cm/s (consistent with a converged handoff from ground-based navigation)
Solar Pressure Model	Spacecraft (SC) with 5 shape components and separate reflective properties	SC Area Scale Factor (SF) Random Bias = 10% SC Area SF Exponentially Correlated Random Variable (ECRV) = 3% with $\tau = 7$ days
Small Forces	SC x-accel = $6.6e-12$ km/s ² SC y-accel = $8.8e-14$ km/s ² SC z-accel = $-3.9e-14$ km/s ²	Accel SF Random Bias = 3% Accel Pointing Random Bias = 3° Accel SF White Noise = 5%
Trajectory Correction Maneuvers	Realized delta-V varies with each trajectory.	Gates Model delta-V Errors: [17] 8.95 mm/s magnitude additive 0.667% magnitude SF 13.5 mm/s direction additive 0.00472 rad pointing

forces perturbing the trajectory resulting from InSight's attitude maintenance [16]. Like SRP, these small forces impact not only the trajectory, requiring periodic trajectory correction maneuvers, but knowledge errors as these small forces degrade overall trajectory estimation and prediction. The InSight project, via experience with the Mars' Phoenix mission that used a similar spacecraft, generated a model with aggregate bias accelerations in each spacecraft body fixed axis direction. The initial bias values were uncertain as well as the associated thrust direction. On top of these initial uncertainties the acceleration magnitudes varied stochastically. As with SRP, we are investigating the ability to replace a tuned body-fixed three axis random bias and stochastic model with a simpler generic model that can robustly maintain filter convergence while still providing sufficient trajectory estimation accuracy to support navigation requirements (i.e., delivery to the top of the Martian atmosphere). The truth acceleration profile used in this study is an earlier version used by the InSight navigation team. Details of these accelerations and the other spacecraft truth models are listed in Table 3.

Trajectory Correction Maneuver (TCM) Targeting and Errors

In the period being investigated (i.e., the last 45 days prior to entry) there are three maneuver opportunities: TCM-4 at E-15 days, TCM-5 at E-8 days, and TCM-6, the final maneuver, at E-22 h. These maneuvers are needed to correct for all of the trajectory perturbations that result from modeling errors from solar pressure, small forces, orbit knowledge errors and execution errors propagating from prior TCMs. Since the current studies focus is on orbit determination and not on the most efficient targeting method, the selected targeting algorithm used for determining the TCMs that

guide the separate truth trajectories to achieving the entry condition is a robust, capable nonlinear least squares optimization algorithm developed by Hanson and Krogh [18]. For simplicity, the targeting is fixed-time, which usually results in higher delta-V costs (more on this later when discussing EFPA results). It is the aim of future work to move to time-variable targeting to minimize TCM magnitudes and switch to a simpler targeting method using K-matrices as described by Maize [19] and demonstrated by JPL’s legacy AutoNav system during Deep Space 1 cruise navigation [20].

Other Models

The other relevant solar system models that an onboard navigation system must use when propagating trajectories, computing observables, and other relevant quantities (such as Mars entry target conditions) include planet, satellite, and asteroid ephemerides and their associated body properties (like mass). Of course, the knowledge of these quantities is imperfect and, as with the other errors discussed previously, they have been injected into the truth simulation. Note that the imaging campaign with the OpNav camera includes 37 different main belt asteroids. These were arrived at by the heuristic asteroid selection algorithm developed by Broschart [10] as being a judicious choice for this trajectory that factors asteroid brightness, camera quality, and asteroid locations plus their associated uncertainties to arrive an optimal mix of asteroids. Additionally, Phobos and Deimos, Mars’ moons, are imaged by the camera – this becomes especially valuable as the spacecraft nears Mars since, with the precise knowledge of Phobos and Deimos orbits relative to Mars, these images provide strong target-relative information. Table 4 has a list of the models, errors, and asteroids.

Radio Tracking and Imaging Campaign

Traditionally in the late cruise near 45 days prior to entry of a Mars lander, DSN tracking is increased to continuous 24/7 support. That is, as each of the DSN stations

Table 4 Truth Models for Solar System Bodies

Parameter	Truth Model	Injected Error (1σ)
Earth/Mars Ephemeris	JPL DE430	DE430 correlated covariance for Earth and Mars
Mars GM	DE430 value	$2.8e-4 \text{ km}^3/\text{s}^2$
Phobos/Deimos Ephemeris	JPL MAR097	0.5 km in each position component
Asteroid Ephemeris	PDS asteroid database for the following asteroids: 2,000,258, 2,004,483, 2,000,140, 2,000,269, 2,001,550, 2,002,577, 2,005,142, 2,002,839, 2,001,432, 2,001,946, 2,000,030, 2,001,627, 2,000,070, 2,000,043, 2,000,172, 2,000,173, 2,000,694, 2,000,951, 2,025,916, 2,001,987, 2,000,198, 2,001,224, 2,000,204, 2,001,235, 2,000,852, 2,000,598, 2,000,475, 2,000,606, 2,000,352, 2,000,353, 2,002,406, 2,001,006, 2,000,112, 2,000,498, 2,000,115, 2,001,147, 2,000,253	PDS asteroid database correlated covariance for each asteroid

rotates into view of the lander a DSN antenna at the complex will collect two-way Doppler and range data between the station and the spacecraft. Typically, only one antenna is in view at a time. However, when two DSN antennas at different complexes are in view of the spacecraft, this data can be augmented with Delta Differenced One-Way Range (DDOR) data (providing ‘plane of sky’ information to complement the ‘line of sight’ data from range and Doppler).

For our onboard navigation case, we replace the two-way range and Doppler with uplink-only one-way CPF-phase and start with this level of support (tracking continuously) but then consider the impact of reducing the DSN support to two hours of transmission from one station per day (vs 24/7 support). Since DDOR is by definition a ground-based data type, it is not considered – instead we use the onboard optical data as a complementary data type. We include only uplink one-way CPF-phase tracking from the in view DSN stations (using a traditional 10° elevation mask). The selected DSN antennas include DSS-15 at Goldstone, California, DSS-45 at Madrid, Spain DSS-65 at Canberra, Australia for the case with continuous tracking. An intriguing question to examine is the impact of reducing this level of tracking. We do so by presenting results when the tracking support is reduced to a single antenna (DSS-65) at 2 h per day, which represents a $\sim 91\%$ reduction in tracking time.

Turning to the onboard, gimballed camera’s imaging campaign, there are four separate cadences that have been programmed. Beginning at E-45 days, 9 to 10 different asteroids (from the set 37 asteroids identified in Table 4) are imaged every 5 days and Phobos and Deimos are imaged every day. The particular asteroids selected for imaging have been determined by a heuristic algorithm developed by Broschart [10]. At E-12, the asteroid imaging frequency increases to 10 daily while Phobos and Deimos also continue to be imaged daily. Then at E-8, the frequency increases to every 6 h. Finally, at E-2 days it is every hour until entry. The images of one target are taken in bursts of 5 images as aid in reducing measurement noise.

Filter Algorithm Selection and Filter Design

The state-of-art navigation filter method for deep space navigation with decades of successful use is the batch sequential linearized Kalman filter (LKF) with iteration using fixed-interval backwards smoothing [21, 22]. Note, iteration is defined as incorporating the LKF solution for an initial state (based on processing an arc of data in a forward pass) into the reference initial state, repropagating the trajectory and variational equations, and then reprocessing the data arc to determine a new trajectory solution. The process repeats to convergence or after a specified number of iterations. To ensure numerical stability the filter must be implemented in a factorized form such as UD or in an upper-triangular Square Root Information Array (SRIF). These methods are well known and have been thoroughly documented in Bierman [21] and implemented in Monte for operational use [12]. It should be noted that the arrival of multiple measurements, at differing times, and with gaps requires modifications to the typical Kalman filtering algorithms which has been documented in Ely [6] and utilized in this study.

A specific question to assess regarding modifications to this traditional filter approach that would make it better suited for onboard use is whether iteration and/or smoothing are required or can a simple forward filter processing multi-week arcs

(45 days in the present case) of observables produce convergent results? Because of significant nonlinearities, it was found that an iterated filter is indeed required and that forward filtering-only with an LKF (with no iteration) yielded biased and divergent solutions. A derivative question to ask, if iteration is required, is smoothing (when stochastic parameters are present) required as well or would backwards mappings suffice? Backwards smoothing to an initial state to iterate an LKF requires significant runtime memory resources that grows with the length and amount of measurement data being processed. Even though efficient smoothing algorithms exist and have been implemented in Monte (see Beirman [22]), they fundamentally require significant storage (relative to a forward filter that is saving only selected solution and covariance data). For an onboard implementation that must iterate, is it possible to linearly map (using the state transition matrix) the LKF solution at the end of a data arc back to the initial epoch, add this to the nominal initial state, and then iterate with the mapped state (vs a smoothed initial state)? Mapping using the state transition matrix is more efficient than smoothing (a single matrix multiply vs many) and doesn't require any additional onboard storage, as the variational equations have already been propagated and stored for use in the forward LKF run. The answer to this question is indeed yes, and will be explored in the results.

Another question to ask is can an extended Kalman filter (EKF) be adapted so that iteration is not required? Recall, that the traditional EKF re-linearizes the nominal trajectory using the filter solution after processing each measurement. The deep space navigation problem is not well suited to this as a single measurement typically does not contain sufficient information to yield solutions with enough accuracy to maintain a stable EKF recursion. This will be quantified later in the results for the EKF simulations. Rather an arc of measurement data must be processed so that sufficient orbit knowledge is gained with the result that the EKF recursion remains stable and yields statistically consistent solutions. In the results, this variant of the EKF is analyzed and compared with the iterated LKF (that maps rather than smooths).

Finally, a pragmatic concern is selecting an optimal data arc length for the LKF before moving the window forward and processing the next arc of data. This selection will need to account for critical events such as TCMs or as delivery to the entry condition nears. Another consideration is there may be insufficient data between the final TCM and entry for a full LKF iteration that initializes with full uncertainties and may need to initialize with the prior covariance (hence, becoming an EKF). These considerations will be examined in future work.

Results and Discussion

The preceding analysis on eliminating calibration data for CPF-phase, reduced-order dynamic modeling for SRP and small forces has led to filter compensation by expanding the onboard filter state to compensate for these modeling errors using stochastic process noise models. An immediate consequence of using reduced-order modeling is the filter cannot be optimally tuned because of the mismatch in the underlying nonlinear models. A simple strategy to account for this mismatch that maintains filter convergence is to apply process noise at values larger than would be required if the truth and nominal nonlinear models did match. In the current application,

this approach was selected by adding generic 3-axis stochastic discrete white noise acceleration parameters to the filter state to compensate for the simplifications used by the onboard modeling (i.e. replacing the multi-component spacecraft model with an attitude independent sphere) and any realized stochastic effects imparted in the truth SRP and small forces from the RCS. A significant finding with this was, if the truth stochastic processes had a non-zero mean, that estimating for these mean values as biases was important for maintaining convergence during the iteration process. This manifested itself specifically in the current scenario with need to include SRP scale factor bias estimation. The onboard filter configuration that was determined to provide the best performance in the presence of these model reductions is listed in Table 5.

Onboard model, CPF-phase only, iterated LKF no smoothing We begin by presenting the Mars approach and entry current state navigation errors and uncertainties when using only CPF-phase data (no OpNav data present) in the case when there is a continuous broadcast of uplink carrier and range signals from whichever of DSS-15/45/65 is in view. The filter model represents the onboard case using only reduced order dynamic models, simple Earth orientations, fitted Earth station trajectories, and predicted long period calibration data for troposphere, UT1, pole motion and using only and predicted calibration data (we'll refer to this as the *onboard model*). The Monte Carlo simulation includes 200 realizations of truth trajectories and the associated set of

Table 5 Onboard Navigation Filter Configuration

Parameter	Filter Parameter Model Type	Uncertainty/Strength (1σ)
Initial Position	Dynamic	1000 km in each component
Initial Velocity	Dynamic	1 km/s
Solar Pressure Scale Factor	Bias	11%
3-Axis Acceleration Noise	Discrete White Noise	1.e-12 km/s ² per day scaled and applied on a 1-h interval in each direction (see Ely [23] p. 309 for details on scaling discrete white noise).
Clock Offset	Bias	1 μ s
Clock Rate	Bias	1.e-14
Phase Ambiguity (& Range Bias)	Per Pass Bias	3 m
Mars GM	Consider	0.00028 km ³ /s ²
Earth Pole Motion	Random Walk	2.4e-11 rad/s ^{1/2} (~ 8 mas/30 days)
Earth UT1	Random Walk	2.5e-6 s/s ^{1/2} (~ 4 ms/30 days)
Earth Station Locations	Bias	10 cm in each component
Dry Troposphere Delay	ECRV	2 cm with $\tau = 3$ h
Wet Troposphere Delay	ECRV	5 cm with $\tau = 0.75$ h
Earth & Mars Ephemerides	Consider	DE430 Earth-Mars Covariance
Phobos & Deimos Ephemerides	Consider	0.5 km in each position component
Asteroid Ephemerides	Off (radio/optical combined) Consider (optical only filter)	PDS Correlated Covariance (position components uncertainties <100 km for all selected asteroids with some as low as 6 km)

CPF-phase observables generated in each realization. In each realization, the onboard filter model is the LKF and starts with the same nominal reference trajectory and processes the data from the realization, and iterates for 3 times. The final iterated current state position errors and associated uncertainties in each position component and associated RSS (in the lower right) are presented in Fig. 3. Shown are the 1- σ and 3- σ uncertainty bounds as well as the filter solution error obtained by differencing the filter solutions (+ reference trajectory) with the truth trajectory. Also listed in the results are statistics of the percentage that a filter solution exceeds the 1- σ and the 3- σ bounds. In the present case, this is 11% and 0.015%, respectively, from a population of 649,200 samples. Assuming ergodic processes and statistics that conform to a normal distribution, one expects 1- σ exceedances to be <31.7% of the time and 3- σ exceedances to be <0.3% of the time, which is true for this case. Another observation with these results is as the spacecraft nears Mars the errors grow until the final few hours when the uncertainties (and errors) drop to less than 150 m. The growth in the error/uncertainty is due primarily to the degrading Earth UT1 and pole motion knowledge when using the months-long predicts. The sudden drop in trajectory uncertainty in the final hours prior to entry is due to the increased information content of the observable as the Mars-centric hyperbolic trajectory changes significantly.

Ground-based model, CPF-phase only, iterated LKF with smoothing It is useful to examine a case that is processing the same data but utilizes the full, high-fidelity spacecraft models, all available daily troposphere delay data, and full high precision Earth frame modeling with UT1 and pole motion daily calibration data (we'll refer to this as the *ground-based model*). In other words, processing the data as if this were ground-based data. With this comparison, we can ascertain the impact of reducing model order and using model predicts vs daily calibration data. The results for this case are shown in Fig. 4. We see that maximum 1- σ and 3- σ uncertainties have dropped from 30 km and 90 km, respectively, at 950 h exhibited in Figs. 3 to 20 km and 60 km.

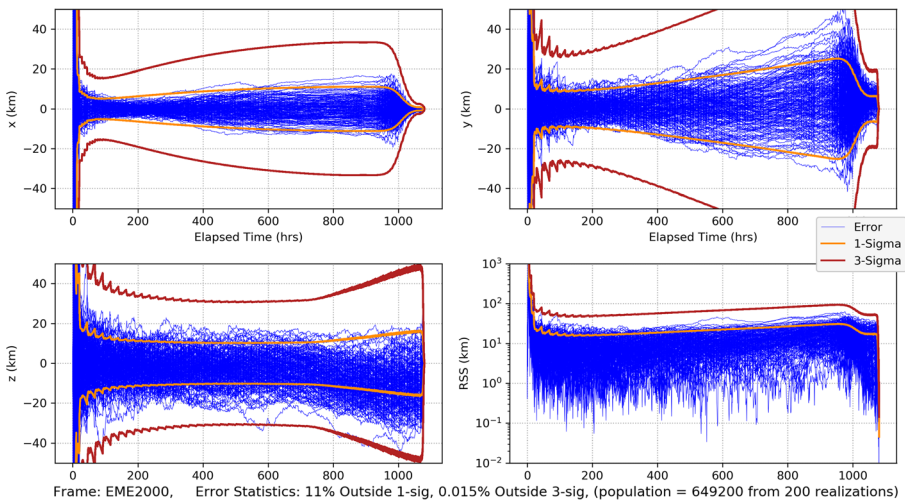


Fig. 3 Mars approach and entry position errors for 200 realizations and uncertainties (1-sigma dark orange, 3-sigma brickred) for case with only uplink one-way CPF-phase data from the DSN when using the *onboard model* and an iterated LKF with no smoothing

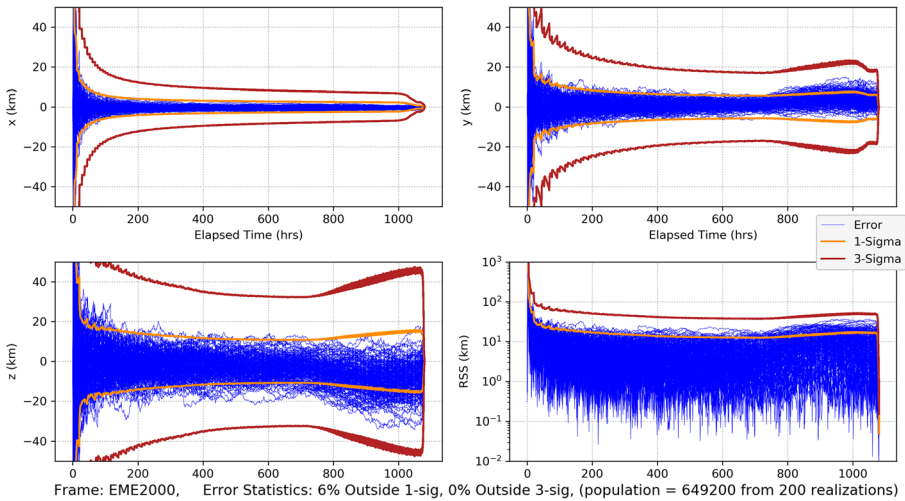


Fig. 4 Same example as shown in Fig. 3 except using high fidelity, *ground-based model* and iterated LKF that *does smooth*

This indicates that the model fidelity reductions employed yield about a 50% increase in overall position uncertainty over most of the cruise. Yet, even with the uncertainty increase seen with the onboard model over much of the cruise, navigation state knowledge at atmosphere entry between the onboard model and that obtained with the high-fidelity ground-based models is similar (hence there is little loss of knowledge at entry when using the onboard, simplified models).

Onboard model, Optical-only, iterated LKF no smoothing The next case examines the case when using only the gimbaled camera OpNav data imaging the 37 asteroids

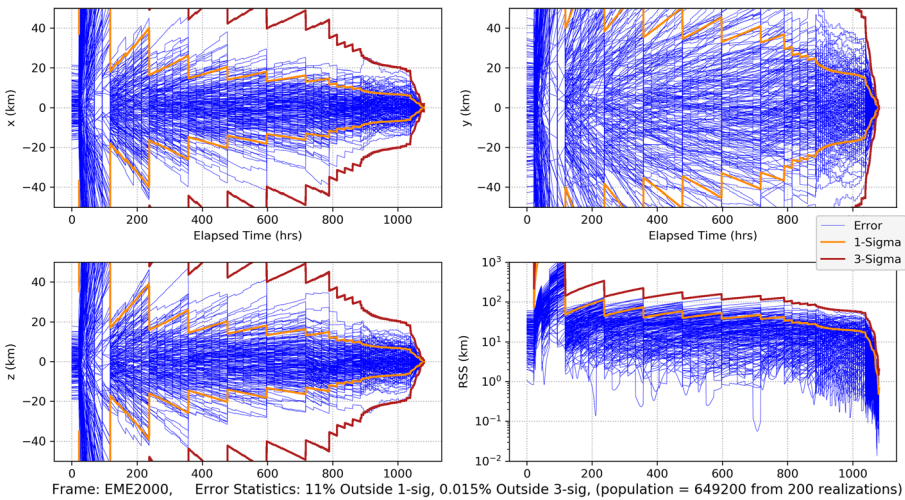


Fig. 5 Mars approach and entry position errors with only optical imaging of asteroids and Phobos and Deimos when using the *onboard model* and an iterated LKF with no smoothing. Additionally, to maintain solution consistency with the uncertainties the asteroid trajectory uncertainties are considered

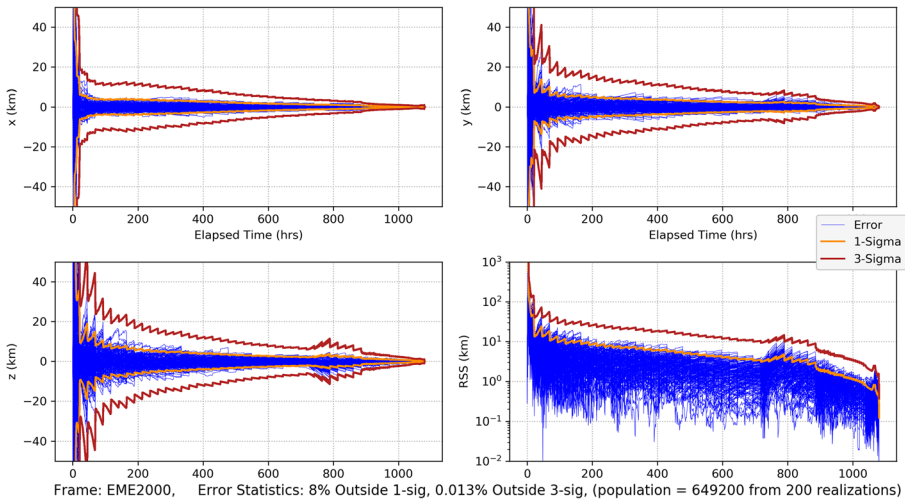


Fig. 6 Mars approach and entry position errors with CPF-phase from the DSN and optical imaging of asteroids and Phobos and Deimos when using the *onboard model* and an iterated LKF with no smoothing

(listed in Table 4) while enroute to Mars as well as Phobos and Deimos. In order to keep the filter errors in line with the formal statistics it is required that the asteroid ephemeris errors need to be considered. This increases the complexity of the onboard filter, but is still tractable (considering the 37 asteroids adds 222 partials that needed to be computed and then used in the consider calculations). The results for this case are shown in Fig. 5. It is clear that the filter errors are consistent with the formal uncertainties with exceedances well below the normal distribution assumptions. Note that sawtooth pattern is a result of imaging every five days, so that between image periods the trajectory errors grow, and then improve when images are taken.

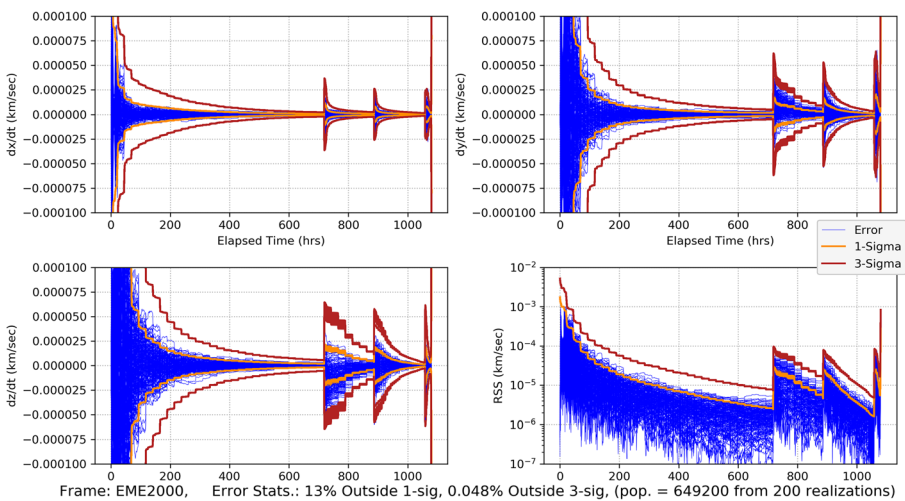


Fig. 7 Mars approach and entry velocity errors with CPF-phase from the DSN and optical imaging of asteroids and Phobos and Deimos when using the *onboard model* and an iterated LKF with no smoothing

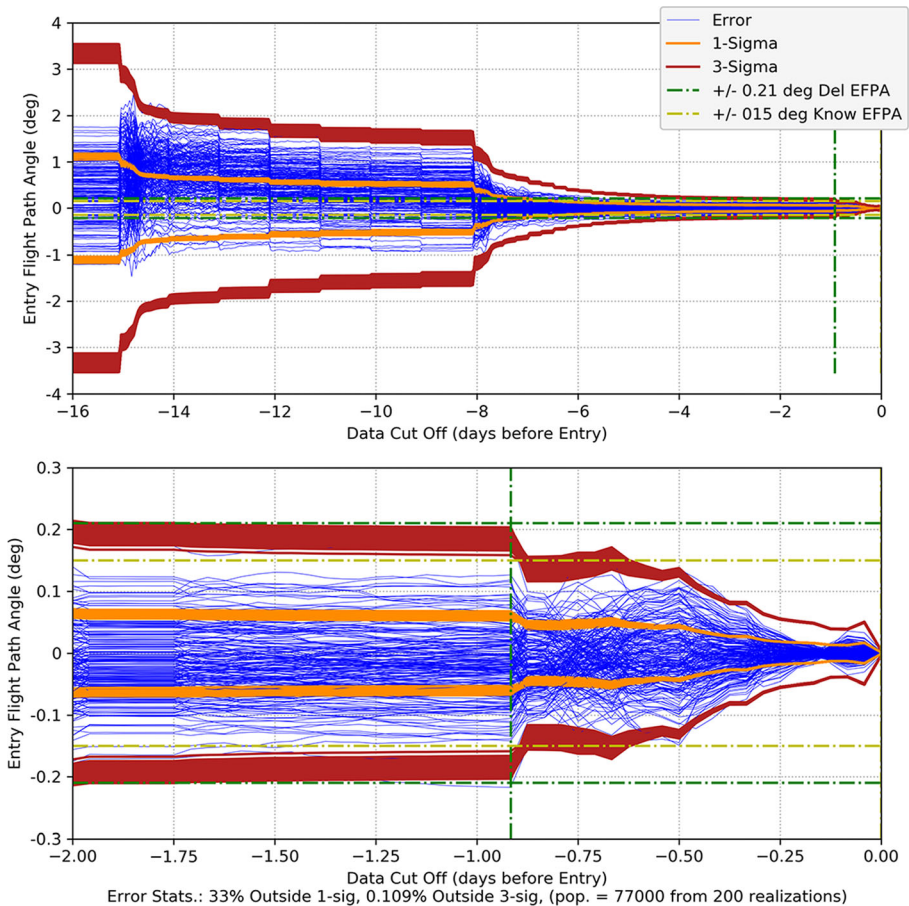


Fig. 8 Mars entry flight path angle as a function of data cut off prior to entry. Top plot is spans from entry-16 days to entry. The bottom plot is for the final two days. Note that the vertical green dash-dot line represents the *onboard* DCO (just before TCM-6) for the delivery EFPA requirement and the vertical yellow dash-dot line represents the DCO (at entry) for the knowledge EFPA

Comparing with the onboard model and CPF-phase only case (Fig. 3), the position formal uncertainties for the optical case are 2 to 3 times larger for most of the cruise, but, as is typical of OpNav, improve as the spacecraft nears Mars. Indeed, at entry the uncertainties are on the order of ~ 2 km ($3\text{-}\sigma$) – compared to <150 m ($3\text{-}\sigma$) for the CPF-phase data only case. Note that with both the CPF-phase only and the optical-only cases, the EFPA knowledge conditions are achieved, but the delivery conditions proved more difficult to meet and were not satisfied. We’ll see next that the combination of the two data types yields sufficient trajectory knowledge to support both the EFPA delivery and knowledge requirements.

Onboard model, CPF-phase combined with optical, iterated LKF no smoothing

We now examine the combination of both data types – CPF-phase and optical – with the onboard processing model. One key difference with the onboard filter model used in this case, relative to the optical-only case, is the asteroid ephemeris errors are not

considered (they are compensated for via use of a conservative image pixel noise value). The reason for doing this is to further simplify the onboard filter. As indicated at the start of this paper, each data type has different geometric sensitivities that are complementary, and should, when combined, improve solutions relative to either alone. The Monte Carlo position errors and associated uncertainties are shown in Fig. 6 and the velocity errors/uncertainties in Fig. 7. Comparing with CPF-phase-only position results in Fig. 3 and the optical-only position results in Fig. 5, the combined data results in Fig. 6 are far more accurate (note that all the position uncertainty results have been plotted on the same scale for clarity). Indeed, the combined results quickly achieve <20 km uncertainties ($3\text{-}\sigma$) in each component, and by the last week <10 km ($3\text{-}\sigma$). The entry knowledge is <200 m ($3\text{-}\sigma$) – a slight degradation from the CPF-phase-only but not significant (the degradation results from considering Phobos/Deimos errors when processing the image data and impacts the Mars-centric state knowledge). Finally, note that there were no perceptible ill effects for not considering the asteroid ephemeris errors.

Maintaining improved position and velocity knowledge should aid in minimizing required delta-V capacity. However, more important is the ability of the onboard navigation to meet the entry flight path angle (EFPA) delivery and knowledge requirements for safe Mars atmosphere entry. Recall that in this case delivery errors need to be $<0.21^\circ$ ($3\text{-}\sigma$). This needs to be achieved by the data cut-off for the final TCM (E-22 h), and knowledge errors from the final navigation state need to be $<0.15^\circ$ ($3\text{-}\sigma$). For ground-based navigation the data cut off for delivery is 1 day before TCM-6 (at E-22 h); however, for onboard navigation this cut-off can be just prior to the maneuver because there is no latency from light time delays or ground-based processing time. Likewise, knowledge errors for ground-based navigation are usually based on the last navigation state obtained at E-6 h and then uploaded to the spacecraft whereas, with onboard navigation, this final state occurs at entry. This represents one of the chief advantages of onboard navigation, having the ability to use navigation knowledge in near real-time vs using solutions with significant latencies. The EFPA as a function of the data cut off (DCO) time prior to entry is shown in Fig. 8 with the bottom plot showing a zoom of the final two days. The results in the final day show that all the realization errors (except for one) and associated $3\text{-}\sigma$ uncertainties lie within the 0.21° delivery limit by the time of TCM-6 (E-22 h). One artifact of using fixed-time targeting is delta-Vs are typically larger in magnitude than with time-variable targeting and, hence, have overall larger execution errors. The EFPA results are dominated by these execution errors; hence, by going to time-variable targeting it is expected that the $3\text{-}\sigma$ delivery EFPA uncertainties at TCM-6 would fall below the requirement with more margin. EFPA knowledge requirements are easily met, and, at $<0.01^\circ$ ($3\text{-}\sigma$), are order of magnitude better than required.

Onboard model, CPF-phase combined with optical, EKF This case is the same as the prior one, but the filter algorithm is now the EKF. As mentioned previously, for an EKF to remain convergent with this class of problem small arcs of data must be processed prior to re-linearizing the reference with the filter solution. For our EKF implementation, we define a data arc as a set number of measurements (vs a period of time). We parametrically explored the number measurements required to achieve consistent and predictable converged filter behavior. We started with 10 measurements,

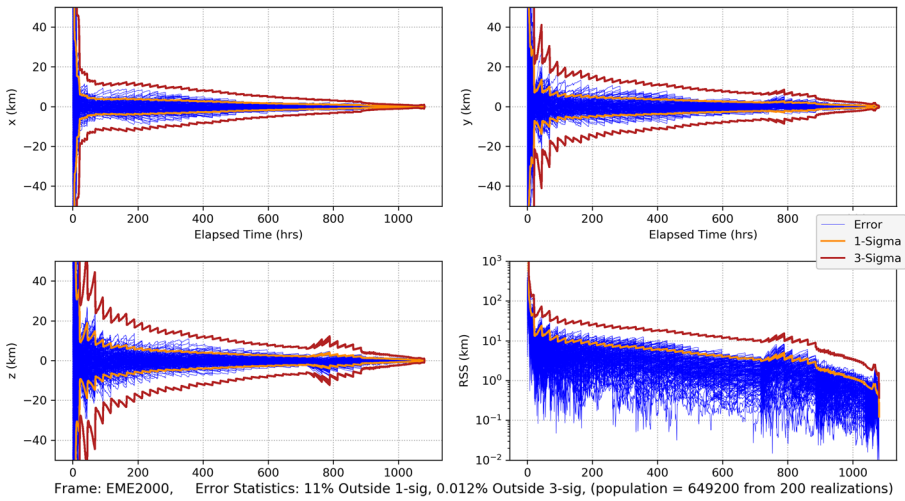


Fig. 9 Mars approach and entry position errors with CPF-phase from the DSN and optical imaging of asteroids and Phobos and Deimos when using the *onboard model* and an EKF with relinearization after every 500 measurements are processed

but it quickly became evident this was insufficient (all filters diverged). At 25 measurements the solutions became well behaved, and produced error statistics for position and velocity that were consistent with the formal uncertainties. The larger the number, the more efficient the filtering approach became. This is because each relinearization forces reintegration, which utilizes computational resources. However, too many measurements and the arc becomes too long and nonlinearities begin to affect convergence, for the current case this was observed at 2000 measurements. Hence, selecting a value between 25 and 2000 would yield accurate answers. For the present case, 500 was

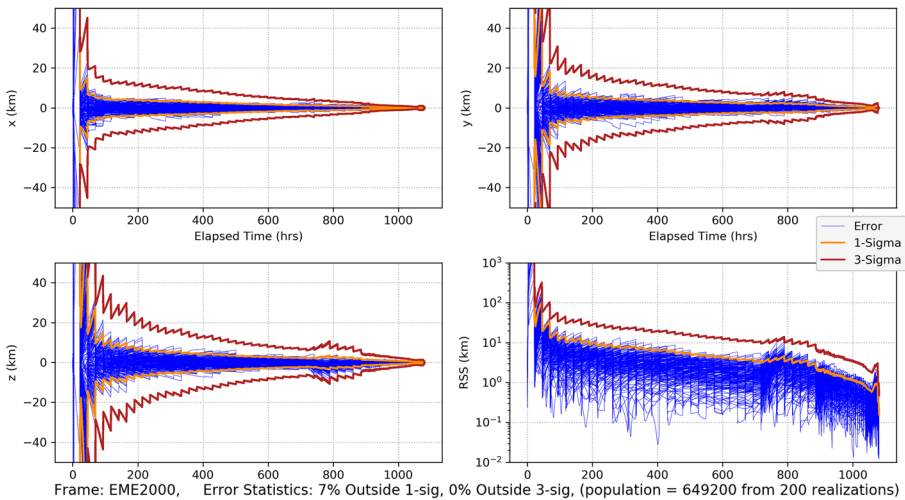


Fig. 10 Mars approach and entry position errors with CPF-phase for only 2 h/day from DSS-65 and optical imaging of asteroids and Phobos and Deimos when using the *onboard model* and an iterated LKF with no smoothing

selected as the best compromise between accuracy and efficiency. It should be noted that this number is now a design parameter, and a different scenario would likely yield a different optimal number of measurements to process before relinearizing. The results for the EKF are shown in Fig. 9. Compared with the results from the LKF in Fig. 6, there is no substantial difference, and indicates that an EKF is a viable alternative to the iterated LKF. However, our experience with this example shows that selecting an EKF requires analysis of a minimal data arc that would be needed to maintain convergence. Additionally, we did encounter some examples with particular realizations that had n -sigma early excursions, that the EKF never recovered, while the iterated LKF with no smoothing always did. Early analysis by Ely [24] examining a Mars orbiting case with onboard models also suggested that the EKF would diverge when initial errors were significant. These observations lead us to recommend the iterated LKF with no smoothing over the EKF for this application.

Onboard model, reduced CPF-phase combined with optical, iterated LKF no smoothing In this final case we examine the impact of reducing the uplink radio tracking from 24/7 to 2 h once per day from a selected DSN station (in this case DSS-65 provides the best observability). One change is we did include asteroid ephemeris estimation into the filter to reduce an observed sensitivity to these errors (the trajectory errors began exceeding the 3-sigma bounds more frequently than typical) in the final days prior to entry. The position errors and uncertainties are shown in Fig. 10. It is evident that there is no significant degradation in performance except in the final day with a small peak in uncertainty. We hypothesize that adding more tracking in the final day would improve accuracy and solution robustness. But even with that additional tracking, this case shows that tracking time could be significantly reduced relative to typical normal ground-based navigation and still safely achieve Mars entry.

Conclusion

In this work we have shown that a novel one-way radiometric data type, called CPF-phase, is suitable for onboard autonomous navigation because it eliminates charged particle effects, a key error source affecting deep space orbit determination. When this data is derived from an onboard, high precision clock, such as DSAC, analysis has shown that minimal calibration data is needed to successfully use it for accurate onboard navigation. Also shown is use of available predictive, long-period models for the Earth troposphere and orientation combined with appropriate filter compensation models to account for real time effects from these errors proved sufficient for maintaining navigation filter convergence.

The research also examined dynamic model simplifications to further simplify the onboard modeling and computations required for effective and accurate autonomous navigation. A representative, high fidelity simulation of Mars cruise and entry navigation was used for evaluating the efficacy of the model considerations. It was found that simplified models are viable in this context, indeed with simple filter process noise compensation a simple ‘cannon ball’ model of the spacecraft was sufficient for meeting Mars’ entry requirements when sufficient measurement data is available.

Filter implementation considerations between using an iterated LKF or an EKF were examined and both were found to be suitable. For the LKF with iteration, it was shown that simply backwards mapping a final state solution to the initial state for iteration versus backwards smoothing to the initial state was satisfactory. This simplification significantly reduces onboard memory and processing requirements. While for the EKF, some batch processing of measurements is still required for maintaining solution convergence where the batch length is a design parameter.

Coupling one-way CPF-phase with onboard optical imaging from a gimballed camera yields navigation solutions for a Mars lander that are sufficiently accurate to enter the Martian atmosphere. Indeed, the combination of the two data types yields solutions that are nearly an order of magnitude more accurate than either by itself. The result is a robust onboard navigation approach that is naturally fault tolerant in the event there are issues with one of the measurement sources. Furthermore, these navigation results are possible while using reduced order models and an iterated LKF *without* smoothing, making the approach amenable for implementation on a resource constrained spacecraft computing system.

Acknowledgements This research was carried out at the Jet Propulsion Laboratory, California Institute of Technology, under a contract with the National Aeronautics and Space Administration. The authors would also like to thank Joseph E. Riedel and William Owen for their input and counsel on this work.

Compliance with Ethical Standards

Conflict of Interest On behalf of all authors, the corresponding author states that there is no conflict of interest.

Open Access This article is licensed under a Creative Commons Attribution 4.0 International License, which permits use, sharing, adaptation, distribution and reproduction in any medium or format, as long as you give appropriate credit to the original author(s) and the source, provide a link to the Creative Commons licence, and indicate if changes were made. The images or other third party material in this article are included in the article's Creative Commons licence, unless indicated otherwise in a credit line to the material. If material is not included in the article's Creative Commons licence and your intended use is not permitted by statutory regulation or exceeds the permitted use, you will need to obtain permission directly from the copyright holder. To view a copy of this licence, visit <http://creativecommons.org/licenses/by/4.0/>.

References

1. Ely, T.A., Burt, E.A., Prestage, J.D., Seubert, J.M., Tjoelker, R.L.: Using the deep space atomic clock for navigation and science. *IEEE Trans. Ultrason. Ferroelectr. Freq. Control.* **65**, 950–961 (Jun. 2018)
2. Bhaskaran, S.: *Autonomous Navigation for Deep Space Missions*. 12th International Conference on Space Operations, Stockholm (2012)
3. McElrath, T., Watkins, M., Portock, B., Graat, E., Baird, D., Wawrzyniak, G.: *Mars Exploration Rovers Orbit Determination Filter Strategy*, AIAA/AAS *Astrodynamics Specialist Conference and Exhibit*. American Institute of Aeronautics and Astronautics, Reston (2004)
4. Moyer, T. D.: *Formulation for Observed and Computed Values of Deep Space Network Data Types for Navigation*, Wiley, (2003)
5. Hofmann-Wellenhof, B., Lichtenberger, H., Wasle, E.: *GNSS Global Navigation Satellite Systems*. Springer-Wien, New York (2008)

6. Ely, T.A., Seubert, J.: Batch Sequential Estimation with Non-uniform Measurements and Non-stationary Noise, pp. 1815–1831. *Advances in the Astronautical Sciences*, Stevenson (2018)
7. Estefan, J. A., Sovers, O. J.: A Comparative Survey of Current and Proposed Tropospheric Refraction-Delay Models for DSN Radio Metric Data Calibration. (1994)
8. Kalarus, M., Schuh, H., Kosek, W., Akyilmaz, O., Bizouard, C., Gambis, D., Gross, R., Jovanović, B., Kumakshv, S., Kutterer, H., Mendes Cerveira, P.J., Pasynok, S., Zotov, L.: Achievements of the earth orientation parameters prediction comparison campaign. *J. Geod.* **84**, 587–596 (2010)
9. Archinal, B.A., Acton, C.H., A'Hearn, M.F., Conrad, A., Consolmagno, G.J., Duxbury, T., Hestroffer, D., Hilton, J.L., Kirk, R.L., Klioner, S.A., McCarthy, D., Meech, K., Oberst, J., Ping, J., Seidelmann, P.K., Tholen, D.J., Thomas, P.C., Williams, I.P.: Report of the IAU Working Group on Cartographic Coordinates and Rotational Elements: 2015. *Celestial Mech. Dynamic. Astron.* **130**, 22 (2018)
10. Broschart, S.B., Bradley, N., Bhaskaran, S.: Kinematic approximation of position accuracy achieved using optical observations of distant asteroids. *J. Spacecr. Rocket.* **56**, 1383–1392 (Jul. 2019)
11. Owen, W.: *Methods of Optical Navigation*, *Advances in the Astronautical Sciences*, Vol. 140, Univelt, (2011)
12. Smith, J., Drain, T., Bhaskaran, S., Martin-Mur, T.: Monte for Orbit Determination. 26th International Symposium on Space Flight Dynamics, Matsuyama (2017)
13. Evans, S., Taber, W., Drain, T., Smith, J., Wu, H.-C., Guevara, M., Sunseri, R., Evans, J.: MONTE: the next generation of mission design and navigation software. *CEAS Space J.* **10**, 79–86 (2018)
14. Sunseri, R. F., Wu, H.-C., Evans, S. E., Evans, J. R., Drain, T. R., and Guevara, M. M.: *Mission Analysis, Operations, and Navigation Toolkit Environment (Monte) Version 040*, (2012)
15. Riedel, J. E., Bhaskaran, S., Desai, S., Han, D., Kennedy, B., McElrath, T., Null, G. W., Ryne, M., Synnott, S. P., Wang, T. C., Werner, R. A., Zamani, E. B.: *Autonomous Optical Navigation. Deep Space 1 Technology Validation Reports*, (2000)
16. Abilleira, F., Halsell, A., Chung, M.-K., Fujii, K., Gustafson, E., Hahn, Y., Lee, J., McPheeters, S.-E., Mottinger, N., Seubert, J., Sklyanskiy, E., Wallace, M.: 2018 Mars Insight Mission Design and Navigation Overview. *AAS/AIAA Astrodynamics Specialist Conference*, Snowbird, UT (2018)
17. Gates, C. R.: A Simplified Model of Midcourse Maneuver Execution Errors, (1963)
18. Hanson, R., Krogh, T.F.: A new algorithm for constrained nonlinear least-squares problems, part 1, (1983)
19. Maize, E. H.: Linear Statistical Analysis of Maneuver Optimization Strategies,” *AAS/AIAA Astrodynamics Specialist Conference*, (1987)
20. Riedel, J. E., Bhaskaran, S., Desai, P. N., Han, D., Kennedy, B., Null, G. W., Synnott, S. P., Wang, T. C., Werner, R. A., Zamani, E. B., McElrath, T., Ryne, M.: *Deep Space 1 Technology Validation Reports: Autonomous Optical Navigation*, (1999)
21. Bierman, G.J.: *Factorization Methods for Discrete Sequential Estimation*. Academic Press, New York (1977)
22. Bierman, G.J.: A new computationally efficient fixed-interval, discrete-time smoother. *Automatica.* **19**, 503–511 (1983)
23. Ely, T.A., Heyne, M., Riedel, J.E.: Altair navigation during trans-lunar cruise, lunar orbit, descent and landing. *J. Spacecr. Rocket.* **49**, 295–317 (2012)
24. Ely, T.A., Veldman, J., Seubert, J.: Preliminary Investigation of Onboard Orbit Determination Using Deep Space Atomic Clock Based Radio Tracking. *AAS/AIAA Space Flight Mechanics Meeting*, Napa (2016)
25. Abilleira, F., Halsell, A., Fujii, K., Gustafson, E., Helfrich, C., Lau, E., Lee, J., Mottinger, N., Seubert, J., Sklyanskiy, E., Wallace, M., Williams, J.: Final Mission and navigation design for the 2016 Mars Insight Mission. *Adv. Astronaut. Sci.* **158**, 1311–1329 (2016)